

# Nonlinear magneto-optical rotation in the presence of radio-frequency field

T. Zigdon,<sup>1</sup> A. D. Wilson-Gordon,<sup>1</sup> S. Guttikonda,<sup>2</sup> E. J. Bahr,<sup>2</sup> O. Neitzke,<sup>3</sup> S. M. Rochester,<sup>3</sup> and D. Budker<sup>3,\*</sup>

<sup>1</sup>*Department of Chemistry, Bar-Ilan University, Ramat Gan 52900, Israel*

<sup>2</sup>*Department of Physics, California State University East Bay, Hayward, California 94542-3084, USA*

<sup>3</sup>*Department of Physics, University of California at Berkeley, Berkeley, California 94720-7300, USA*

[\\*budker@berkeley.edu](mailto:budker@berkeley.edu)

**Abstract:** We report measurements of nonlinear magneto-optical rotation (NMOR) for the D<sub>2</sub> line of <sup>87</sup>Rb atoms in an antirelaxation-coated vapor cell in the presence of a radio-frequency (rf) field. The experimental NMOR signals as a function of rf field frequency for various rf field powers are compared to a theoretical model based on the density-matrix formalism. The comparison between experiment and theory enables understanding of the ground-state atomic spin polarization dynamics, illustrated using plots of the probability distribution of the atomic angular momentum.

© 2021 Optical Society of America

**OCIS codes:** (020.0020) Atomic and molecular physics; (020.3690) Line shapes and shifts; (020.7490) Zeeman effect

---

## References and links

1. A. Kastler, *J. Phys. Radium* **11**, 225 (1950).
2. C. Cohen-Tannoudji, *Atoms in Electromagnetic Fields* (World Scientific, Singapore, 1994).
3. T. G. Walker and W. Happer, "Spin-exchange optical pumping of noble-gas nuclei," *Rev. Mod. Phys.* **69**, 629 (1997).
4. A. I. Okunevich, *Opt. Spectrosc.* **97**, 834841 (2004).
5. D. F. Jackson Kimball, L. R. Jacome, S. Guttikonda, E. J. Bahr, and L. F. Chan, "Magnetometric sensitivity optimization for nonlinear optical rotation with frequency-modulated light: Rubidium D2 line," *J. Appl. Phys.* **106**, 063113 (2009).
6. D. Budker, D. F. Kimball, S. M. Rochester, V. V. Yashchuk, and M. Zolotarev, "Sensitive magnetometry based on nonlinear magneto-optical rotation," *Phys. Rev. A* **62**, 043403 (2000).
7. D. Budker, W. Gawlik, D. F. Kimball, S. M. Rochester, V. V. Yashchuk, and A. Weiss, "Electric-field-induced change of the alkali-metal vapor density in paraffin-coated cells," *Rev. Mod. Phys.* **74**, 1153 (2002).
8. V. V. Yashchuk, D. Budker, W. Gawlik, D. F. Kimball, Y. P. Malakyan, and S. M. Rochester, "Selective addressing of high-rank atomic polarization moments," *Phys. Rev. Lett* **90**, 253001 (2003).
9. S. Pustelny, D. F. J. Kimball, S. M. Rochester, V. V. Yashchuk, W. Gawlik, and D. Budker, "Pump-probe nonlinear magneto-optical rotation with frequency-modulated light," *Phys. Rev. A* **73**, 023817 (2006).
10. V. M. Acosta, M. Auzinsh, W. Gawlik, P. Grisins, J. M. Higbie, D. F. Jackson Kimball, L. Krzemien, M. P. Ledbetter, S. Pustelny, S. M. Rochester, V. V. Yashchuk, and D. Budker, "Electric-field-induced change of the alkali-metal vapor density in paraffin-coated cells," *Opt. Express* **16**, 11423 (2008).
11. S. Xu, S. M. Rochester, V. V. Yashchuk, M. H. Donaldson, and D. Budker, "Construction and applications of an atomic magnetic gradiometer based on nonlinear magneto-optical rotation," *Rev. Sci. Instrum.* **77**, 083106 (2006).
12. A. Garroway, M. Buess, J. Miller, B. Suits, A. Hibbs, G. Barrall, R. Matthews, and L. Burnett, *IEEE Trans. Geosci. Remote Sens.* **39**, 1108 (2001).
13. S. Xu, V. V. Yashchuk, M. H. Donaldson, S. M. Rochester, D. Budker, and A. Pines, "Magnetic resonance imaging with an optical magnetometer," *Proc. Nat. Acad. Sci. (USA)* **10.1073**, 0605396103 (2006).

14. R. Bradley, J. Clarke, D. Kinion, L. J. Rosenberg, K. Bibber, S. Matsuki, M. Muck, and P. Sikivie, “Microwave cavity searches for dark-matter axions,” *Rev. Mod. Phys.* **75**, 777 (2003).
15. M. P. Ledbetter, V. M. Acosta, S. M. Rochester, D. Budker, S. Pustelny, and V. V. Yashchuk, “Detection of radio-frequency magnetic fields using nonlinear magneto-optical rotation,” *Phys. Rev. A* **75**, 023405 (2007).
16. W. Wasilewski, K. Jensen, H. Krauter, J. J. Renema, M. V. Balabas, and E. S. Polzik, “Quantum noise limited and entanglement-assisted magnetometry,” *Phys. Rev. Lett.* **104**, 133601 (2010).
17. W. Chalupczak, P. Josephs-Franks, S. Pustelny, and W. Gawlik, “Optical–radio-frequency resonances free from power broadening,” *Phys. Rev. A* **81**, 013422 (2010).
18. J. Brossel and F. Bitter, “A new “double resonance” method for investigating atomic energy levels. Application to  $\text{Hg } ^3P_1^*$ ,” *Phys. Rev.* **86**, 308–316 (1952).
19. D. F. Jackson Kimball, O. Neitzke, E. J. Bahr, S. Guttikonda, S. M. Rochester, M. P. Ledbetter, I. Novikova, B. Coste, S. A. Rangwala, J. M. Higbie, A. I. Okunevich, V. V. Yashchuk, and D. Budker (in preparation).
20. M. A. Bouchiat and J. Brossel, “Relaxation of optically pumped Rb atoms on paraffin-coated walls,” *Phys. Rev.* **147**, 41–54 (1966).
21. D. Budker, V. Yashchuk, and M. Zolotarev, “Nonlinear magneto-optic effects with ultranarrow widths,” *Phys. Rev. Lett.* **81**, 5788–5791 (1998).
22. M. T. Graf, D. F. Kimball, S. M. Rochester, K. Kerner, C. Wong, D. Budker, E. B. Alexandrov, M. V. Balabas, and V. V. Yashchuk, “Relaxation of atomic polarization in paraffin-coated cesium vapor cells,” *Phys. Rev. A* **72**, 023401 (2005).
23. K. L. Corwin, Z.-T. Lu, C. F. Hand, R. J. Epstein, and C. E. Wieman, “Frequency-stabilized diode laser with the Zeeman shift in an atomic vapor,” *Appl. Opt.* **37**, 3295 (1998).
24. V. Yashchuk, D. Budker, and J. Davis, “Laser frequency stabilization using linear magneto-optics,” *Rev. Sci. Instr.* **71**, 341 (2000).
25. D. Budker, D. Kimball, S. Rochester, and V. Yashchuk, “Nonlinear magneto-optical rotation via alignment-to-orientation conversion,” *Phys. Rev. Lett.* **85**, 2088 (2000).
26. M. Auzinsh, “Angular momenta dynamics in magnetic and electric field: Classical and quantum approach,” *Can. J. Phys.* **75**, 853–872 (1997).
27. S. M. Rochester and D. Budker, “Atomic polarization visualized,” *Am. J. Phys.* **69**, 450–4 (2001).
28. M. Auzinsh, D. Budker, and S. M. Rochester, *Optically Polarized Atoms: Understanding Light-Atom Interactions* (Oxford University Press, Oxford, 2010).
29. S. I. Kanorsky, A. Weis, J. Wurster, and T. W. Hänsch, “Quantitative investigation of the resonant nonlinear faraday effect under conditions of optical hyperfine pumping,” *Phys. Rev. A* **47**, 1220–6 (1993).
30. E. B. Alexandrov, M. Auzinsh, D. Budker, D. F. Kimball, S. M. Rochester, and V. V. Yashchuk, “Dynamic effects in nonlinear magneto-optics of atoms and molecules: review,” *J. Opt. Soc. Am. B* **22**, 7 (2005).

## 1. Introduction

The dynamics of atomic spin polarization in the presence of radio-frequency (rf) fields has been extensively studied (for example, see [1, 2, 3, 4]). Recently, it has been demonstrated that nonlinear magneto-optical rotation (NMOR) is a sensitive probe of atomic spin dynamics [5, 6, 7], and can in fact be used to selectively create and probe different multipole moments of the atomic spin polarization [8, 9, 10]. There are numerous practical applications for the use of NMOR to detect the response of atomic spins to rf fields: for example, in nuclear magnetic resonance (NMR) [11], including nuclear quadruple resonance (NQR) [12], and magnetic resonance imaging (MRI) [13] experiments. One can also use such methods in tests of fundamental physics [14]. In our previous research, we built an alkali-vapor magnetometer for the detection of rf fields [15]. Recent work by researchers using a similar experimental setup is described in Refs. [16, 17]. The experiment [15] demonstrated a sensitivity to oscillating magnetic fields of  $100 \text{ pG}/\sqrt{\text{Hz}}$ . The line shapes observed in the magnetometry experiment in the limit of low rf power are well understood. However, when higher-strength rf fields are applied, nontrivial line shapes are seen, with similarities to those of the “Majorana-Brossel effect” in double-resonance spectroscopy [18]. We have conducted experimental and theoretical investigations to explain the mechanism that produces these line shapes.

In this work we present experimental NMOR signals taken on the  $D_2$  line of  $^{87}\text{Rb}$  atoms contained in an antirelaxation-coated cell in the presence of an rf field. The signals are primarily due to interaction with the  $F_g = 2 \rightarrow F_e = 1$  transition (the subscripts  $g$  and  $e$  indicate the

ground and excited states, respectively). They are compared to a theoretical model based on the density-matrix formalism. The theoretical model, which is found to be in good agreement with experimental results, enables the understanding of the underlying atomic spin dynamics and their relationship to the detected NMOR signals. The character of the observed line shapes is found to be different depending on the value of the Rabi frequency for the rf field,  $\Omega_{\text{rf}}$ , relative to the ground-state atomic-polarization relaxation rate  $\gamma_l$  and the magnetic resonance frequency  $\Omega_L$ . This work is motivated by an ongoing project aimed at measuring collisional transfer of alignment in collisions between different ground-state alkali atoms [19].

## 2. Description of the experiment and theory

### 2.1. Description of experiment

The experiment employs a spherical paraffin-coated glass vapor cell (diameter = 10 cm) filled with a natural isotopic mixture of rubidium. The cell coating allows polarization of ground-state alkali atoms to survive several thousand wall collisions [20, 21], thereby extending the lifetime of atomic polarization. The cell is heated by a constant air stream from a heat exchanger. During all measurements in this work the temperature of the cell is stabilized at  $\approx 41^\circ\text{C}$ , resulting in a Rb vapor density of  $7.2(7) \times 10^{10}$  atoms per  $\text{cm}^3$ . The density was extracted from fitting a low-light power ( $\approx 8 \mu\text{W}$ ) transmission spectrum for the Rb  $D_2$  line to a calculated spectrum assuming linear absorption. Under these experimental conditions the longitudinal relaxation rate of ground-state alignment of the isotope  $^{87}\text{Rb}$  was measured to be  $31.7(7) \text{ s}^{-1}$ . The value represents the effective relaxation rate of alignment polarization due to diverse types of atomic collisions occurring in the vapor cell, e.g. electron-randomization collisions with the wall, uniform relaxation due to the reservoir effect and spin-exchange collisions among Rb atoms [22]. A four-layer  $\mu$ -metal magnetic shield (see Fig. 1) surrounds the vapor cell and reduces the external magnetic field by a factor of  $\sim 10^6$  [21]. Additionally, three orthogonal solenoidal coils placed inside the innermost shield are used to compensate residual magnetic fields to below 1  $\mu\text{G}$  and to create additional static and oscillating fields. For our measurements we apply a static magnetic field  $\mathbf{B}_0$  in the  $\hat{z}$  direction (typical strength  $B_0 = 0.8 \text{ mG}$ ) and an oscillating magnetic field  $\mathbf{B}_{\text{rf}} = B_{\text{rf}}\hat{x}\cos\omega_{\text{rf}}t$  along the  $x$ -axis (typical amplitude up to  $B_{\text{rf}} = 0.25 \text{ mG}$ ) using the sine wave output of a lock-in amplifier.

A laser beam, initially polarized along the  $z$ -axis, propagates through the vapor cell in the  $\hat{y}$  direction. The beam is generated by a distributed feedback (DFB) laser, which is tuned to the red wing of the  $F_g = 2 \rightarrow F_e = 1$  transition in the 780 nm  $D_2$  line of  $^{87}\text{Rb}$ . The wavelength is locked using a dichroic atomic vapor laser lock [23, 24]. The light intensity is 10  $\mu\text{W}$  throughout the measurements and the beam diameter is  $\approx 2 \text{ mm}$ . Linear dichroism of the atomic medium induces changes in the light polarization. (For high light power, the medium can also acquire circular birefringence [25].) After transmission through the vapor cell the polarization of the light beam is analyzed using a balanced polarimeter setup, consisting of a polarizing beam splitter (Rochon crystal) and two photodiodes detecting the intensities of the two beams exiting the crystal. The component of the difference signal that oscillates at the frequency of the rf field is then extracted by the lock-in amplifier.

Experimental signals as a function of rf frequency, along with predictions of the theory described in Sec. 2.2, are given in Fig. 2 for different amplitudes of the rf field. At the lowest amplitudes, the observed line shapes are Lorentzians, while for higher amplitudes, additional features are seen.

### 2.2. Description of theory

The experimental signal is primarily due to interaction with the  $F_g = 2 \rightarrow F_e = 1$  transition of the  $D_2$  line of  $^{87}\text{Rb}$ , although there are also contributions from the  $F_g = 2 \rightarrow F_e = 2$  and

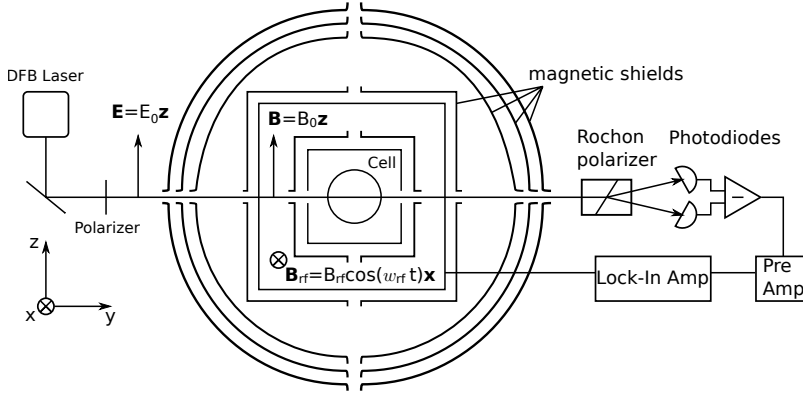


Fig. 1. A laser beam linearly polarized along the  $z$  axis propagates through a paraffin-coated vapor cell, producing ground-state alignment in the  $^{87}\text{Rb}$  atoms. A constant magnetic field  $\mathbf{B}_0$  and an oscillating rf magnetic field  $\mathbf{B}_{\text{rf}}$  are applied within the magnetic shield that surrounds the cell. A balanced polarimeter and lock-in amplifier are used to analyze polarization rotation of the light induced by the atoms. A resonance is observed when the rf frequency is equal to the ground-state Larmor frequency of the atoms.

$F_g = 2 \rightarrow F_e = 3$  transitions. Theoretical modeling shows that signals produced on each of these transitions have similar line shapes, although the signal from a  $F_g = 2 \rightarrow F_e = 3$  transition is of the opposite sign. In fact, the effects that we describe here are present for any transition with ground-state angular momentum  $F_g \geq 1$ . For the theoretical treatment presented here, we therefore consider the simplest case of a  $F_g = 1 \rightarrow F_e = 0$  transition, for which analytical solutions are readily obtained. The model for this system gives results in reasonable agreement with the experimental data, indicating that the effects are not strongly dependent on the angular momenta characterizing the transition.

The atoms are subject to a  $\hat{z}$ -directed field  $\mathbf{B}_0 = B_0\hat{z}$ , corresponding to the Larmor frequency  $\Omega_L = g\mu_B B_0$ , where  $\mu_B$  is the Bohr magneton and  $g$  is the Landé factor (we set  $\hbar = 1$ ). Linearly polarized light propagating in the  $\hat{y}$  direction with polarization in the  $\hat{z}$  direction optically pumps the system and creates an aligned state. An oscillating rf magnetic field is applied in the  $\hat{x}$  direction,  $\mathbf{B}_{\text{rf}} = B_{\text{rf}}\hat{x}\cos\omega_{\text{rf}}t$ , corresponding to the rf Rabi frequency  $\Omega_{\text{rf}} = g\mu_B B_{\text{rf}}$ . The dependence on  $\Omega_{\text{rf}}$  of the rf line shape of the optical rotation signal is studied. An analytic solution can be obtained in case in which the rf power is low enough that the rf power-broadened line width is much smaller than  $\Omega_L$  and  $\omega_{\text{rf}}$ . Numerical solutions are obtained in the general case.

The experiment is performed using a vapor cell with an antirelaxation coating. In such a cell, atoms can be optically pumped in the light beam and then exit and return to the beam after undergoing collisions with the cell walls, without the polarization relaxing. Thus a complete theoretical description must take into account the different conditions—and the different state of the atoms—inside and outside the beam. If the light power is low enough so that saturation effects do not occur in the beam, however, the system can be modeled by considering the average state of the atoms over the entire cell. This amounts to mapping the case of a coated cell onto that of an uncoated cell (i.e., one in which atomic polarization can be considered to completely relax as soon as the atoms leave the light beam). The light beam in the uncoated cell is taken to have an intensity equal to the average intensity over the entire cross-section of the coated cell, and the atomic transit rate through the beam is taken to be equal to the ground-state polarization relaxation rate in the coated cell. (This “effective” uncoated cell must be very

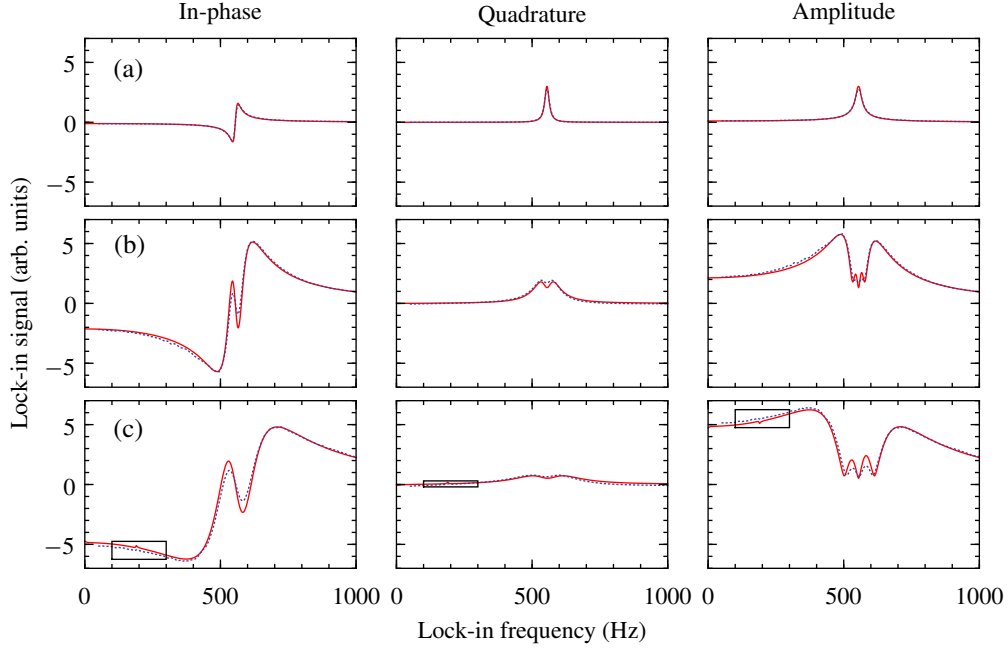


Fig. 2. Experimental spectra (dotted lines) and theoretical predictions (solid lines) for three different values of the rf field amplitude. The experimental values (obtained from calibrated measurements of the coil current) in terms of the Rabi frequency  $\Omega_{\text{rf}}$  are (a)  $\Omega_{\text{rf}}/(2\pi) = 3$  Hz, (b)  $\Omega_{\text{rf}}/(2\pi) = 63$  Hz, (c)  $\Omega_{\text{rf}}/(2\pi) = 158$  Hz. These values are used in the theory, along with the parameters natural width  $\Gamma = 2\pi \times 6.1 \mu\text{s}^{-1}$  (chosen equal to the natural width of the Rb  $D_2$  transition), light power  $5 \mu\text{W}$ , ground-state relaxation rate  $\gamma = 2\pi \times 8 \text{ s}^{-1}$ , and bias-field Larmor frequency  $\Omega_L/(2\pi) = 554.75$  Hz. These last three parameters are chosen for optimal agreement with the data—they are reasonably close to the experimental values. The value for light power is applied to the theoretical model using the method described in Sec. 2.2. At low rf-field strengths, as in row (a), the spectra are Lorentzians. An additional central feature appears in the resonances when  $\Omega_{\text{rf}}$  exceeds  $\gamma$ , as in rows (b) and (c). Boxes in row (c) indicate regions plotted on expanded scales in Fig. 3.

large, in order to account for the slow ground-state relaxation of the coated cell.) This is the case that we will consider.

Another complication arising in a complete model of an atomic vapor cell is the velocity dependence of the atomic state due to Doppler broadening and collisional velocity mixing effects. These effects tend to change the dependence of a signal on the light frequency. Since we hold the light frequency fixed in this experiment, the main effect is the introduction of an overall scaling factor. Therefore, we neglect the velocity dependence in our model.

In the Zeeman basis  $\{|F_g = 1, m = 1\rangle, |F_g = 1, m = 0\rangle, |F_g = 1, m = -1\rangle, |F_e = 0, m = 0\rangle\}$ , the total time-dependent Hamiltonian  $H$  of the Doppler-free system under the optical rotating-wave approximation is

$$H = \begin{pmatrix} \Omega_L & \frac{\Omega_{\text{rf}}}{2\sqrt{2}}(e^{i\omega_{\text{rf}}t} + e^{-i\omega_{\text{rf}}t}) & 0 & 0 \\ \frac{\Omega_{\text{rf}}}{2\sqrt{2}}(e^{i\omega_{\text{rf}}t} + e^{-i\omega_{\text{rf}}t}) & 0 & \frac{\Omega_{\text{rf}}}{2\sqrt{2}}(e^{i\omega_{\text{rf}}t} + e^{-i\omega_{\text{rf}}t}) & -\frac{\Omega_R}{2\sqrt{3}} \\ 0 & \frac{\Omega_{\text{rf}}}{2\sqrt{2}}(e^{i\omega_{\text{rf}}t} + e^{-i\omega_{\text{rf}}t}) & -\Omega_L & 0 \\ 0 & -\frac{\Omega_R}{2\sqrt{3}} & 0 & -\Delta \end{pmatrix}, \quad (1)$$

where  $\Omega_R$  is the Rabi frequency of the optical transition induced by the linearly polarized light and  $\Delta = \omega - \omega_0$  is the optical detuning;  $\omega$  is the frequency of the light and  $\omega_0$  is the frequency of the ground to excited state transition in the absence of a magnetic field. For the case in which the ground-state relaxation rate and  $\Omega_{\text{rf}}$  are both much smaller than  $\Omega_L$  and  $\omega_{\text{rf}}$ , we can also perform the rotating-wave approximation on the rf field, in order to remove the Larmor-frequency time dependence from the Hamiltonian. In the rotating frame obtained using the unitary transformation

$$U(t) = \begin{pmatrix} e^{-i\omega_{\text{rf}}t} & 0 & 0 & 0 \\ 0 & 1 & 0 & 0 \\ 0 & 0 & e^{i\omega_{\text{rf}}t} & 0 \\ 0 & 0 & 0 & 1 \end{pmatrix}, \quad (2)$$

the density-matrix evolution can be written in terms of an effective Hamiltonian  $H' = U^{-1}HU - iU^{-1}\frac{dU}{dt}$ . After dropping fast-oscillating, off-resonant terms, we have

$$H' = \begin{pmatrix} -\Delta_{\text{rf}} & \frac{\Omega_{\text{rf}}}{2\sqrt{2}} & 0 & 0 \\ \frac{\Omega_{\text{rf}}}{2\sqrt{2}} & 0 & \frac{\Omega_{\text{rf}}}{2\sqrt{2}} & -\frac{\Omega_R}{2\sqrt{3}} \\ 0 & \frac{\Omega_{\text{rf}}}{2\sqrt{2}} & \Delta_{\text{rf}} & 0 \\ 0 & -\frac{\Omega_R}{2\sqrt{3}} & 0 & -\Delta \end{pmatrix}, \quad (3)$$

where  $\Delta_{\text{rf}} = \omega_{\text{rf}} - \Omega_L$  is the rf detuning. The evolution of the density matrix  $\rho$  (normalized so that  $\text{Tr}\rho = 1$ ) is described by the Liouville equation

$$\dot{\rho} = -i[H', \rho] - \frac{1}{2}\{\zeta, \rho\} + \Lambda, \quad (4)$$

where  $[\ ]$  denotes the commutator and  $\{\ }$  the anticommutator. The relaxation of the system is given by the matrix

$$\zeta = \begin{pmatrix} \gamma & 0 & 0 & 0 \\ 0 & \gamma & 0 & 0 \\ 0 & 0 & \gamma & 0 \\ 0 & 0 & 0 & \Gamma + \gamma \end{pmatrix}, \quad (5)$$

where the excited state decays spontaneously with a rate  $\Gamma$  and the ground and excited states relax with a rate  $\gamma_l$  due to the exit of atoms from the light beam. The matrix  $\Lambda$  describes re-population of the ground state due to atoms entering the beam and spontaneous decay from the upper state, and is given by

$$\Lambda = \begin{pmatrix} \frac{\gamma_l}{3} + \frac{\Gamma}{3}\rho_{e_0e_0} & 0 & 0 & 0 \\ 0 & \frac{\gamma_l}{3} + \frac{\Gamma}{3}\rho_{e_0e_0} & 0 & 0 \\ 0 & 0 & \frac{\gamma_l}{3} + \frac{\Gamma}{3}\rho_{e_0e_0} & 0 \\ 0 & 0 & 0 & 0 \end{pmatrix}, \quad (6)$$

where the Zeeman ground and excited sublevels are denoted as  $g_{m_g}$  and  $e_{m_e}$ , and  $\rho_{e_0e_0}$  is the population in the excited state.

Under the rotating-wave approximation for the rf field described above, the evolution equations for the rotating-frame density matrix contain no explicit time dependence. We can therefore set the time derivatives to zero and solve the resulting system of linear equations for the steady state. Taking the case of low light power, we solve the equations to third order in the optical Rabi frequency, which is the lowest order at which nonlinear optical rotation signals appear. Using the inverse transformation  $U^{-1}$ , we transform back to the laboratory frame to find the time-dependent density matrix.

The expectation value of the medium polarization is found from the laboratory-frame density matrix. By substituting this value into the wave equation, we can calculate the optical-rotation signal measured in the laboratory frame in terms of the rotating-frame density-matrix elements. After multiplying by the reference signal and averaging over time, we find the in-phase and quadrature (out-of-phase) signals per unit length  $d\ell$  of the medium to be

$$\frac{\partial \varphi^{\text{in}}}{\partial \ell} = -\frac{\sqrt{\frac{3}{2}}N\Gamma\lambda^2}{4\pi\Omega_R} \text{Im}(\rho_{e_0g_{-1}} - \rho_{e_0g_1}), \quad (7)$$

$$\frac{\partial \varphi^{\text{out}}}{\partial \ell} = \frac{\sqrt{\frac{3}{2}}N\Gamma\lambda^2}{4\pi\Omega_R} \text{Re}(\rho_{e_0g_{-1}} + \rho_{e_0g_1}), \quad (8)$$

where  $\lambda$  is the transition wavelength,  $N$  is the atomic density, and  $\rho_{e_0g_{-1}}$  and  $\rho_{e_0g_1}$  are the optical coherences between the excited state and the ground  $g_{-1}$  and  $g_1$  Zeeman sublevels, respectively. The magnitude of the optical-rotation signal is given by

$$\begin{aligned} \frac{\partial \varphi^{\text{abs}}}{\partial \ell} &= \sqrt{\left(\frac{\partial \varphi^{\text{in}}}{\partial \ell}\right)^2 + \left(\frac{\partial \varphi^{\text{out}}}{\partial \ell}\right)^2} \\ &= \frac{\sqrt{\frac{3}{2}}N\Gamma\lambda^2}{4\pi\Omega_R} \{[\text{Im}(\rho_{e_0g_{-1}} - \rho_{e_0g_1})]^2 + [\text{Re}(\rho_{e_0g_{-1}} + \rho_{e_0g_1})]^2\}^{1/2}. \end{aligned} \quad (9)$$

The expressions obtained after substituting in the solution for the density matrix are complicated; to simplify the presentation we assume that the light field is on resonance and that  $\Gamma$  is much greater than all other rates in the problem. This gives

$$\frac{\partial \varphi^{\text{in}}}{\partial \ell} = \frac{N\Delta_{\text{rf}}\lambda^2\Omega_{\text{rf}}(2\gamma_l^2 + 8\Delta_{\text{rf}}^2 - \Omega_{\text{rf}}^2)\Omega_R^2}{36\pi\Gamma\gamma_l(\gamma_l^2 + 4\Delta_{\text{rf}}^2 + \Omega_{\text{rf}}^2)[4(\gamma_l^2 + \Delta_{\text{rf}}^2) + \Omega_{\text{rf}}^2]}, \quad (10)$$

$$\frac{\partial \varphi^{\text{out}}}{\partial \ell} = \frac{N\lambda^2\Omega_{\text{rf}}(4\gamma_l^2 + 16\Delta_{\text{rf}}^2 + \Omega_{\text{rf}}^2)\Omega_R^2}{72\pi\Gamma(\gamma_l^2 + 4\Delta_{\text{rf}}^2 + \Omega_{\text{rf}}^2)[4(\gamma_l^2 + \Delta_{\text{rf}}^2) + \Omega_{\text{rf}}^2]}, \quad (11)$$

where we have neglected the contribution to optical rotation that is independent of the light power. Expanding these expressions in a power series in  $\Omega_{\text{rf}}$ , we obtain

$$\frac{\partial \varphi^{\text{in}}}{\partial \ell} = \frac{N\Delta_{\text{rf}}\lambda^2\Omega_R^2}{72\pi\Gamma\gamma(\gamma^2 + \Delta_{\text{rf}}^2)}\Omega_{\text{rf}} - \frac{N\Delta_{\text{rf}}\lambda^2\Omega_R^2(7\gamma^2 + 10\Delta_{\text{rf}}^2)}{288\pi\Gamma\gamma(\gamma^2 + \Delta_{\text{rf}}^2)(\gamma^2 + 4\Delta_{\text{rf}}^2)}\Omega_{\text{rf}}^3 + O[\Omega_{\text{rf}}]^5, \quad (12)$$

$$\frac{\partial \varphi^{\text{out}}}{\partial \ell} = \frac{N\lambda^2\Omega_R^2}{72\pi\Gamma(\gamma^2 + \Delta_{\text{rf}}^2)}\Omega_{\text{rf}} - \frac{N\lambda^2\Omega_R^2(4\gamma^2 + 7\Delta_{\text{rf}}^2)}{288\pi\Gamma(\gamma^2 + \Delta_{\text{rf}}^2)(\gamma^2 + 4\Delta_{\text{rf}}^2)}\Omega_{\text{rf}}^3 + O[\Omega_{\text{rf}}]^5, \quad (13)$$

$$\frac{\partial \varphi^{\text{abs}}}{\partial \ell} = \frac{N\lambda^2\Omega_R^2\Omega_{\text{rf}}}{144\pi\Gamma\gamma\sqrt{\gamma^2 + \Delta_{\text{rf}}^2}} - \frac{N\lambda^2(2\gamma^2 + 5\Delta_{\text{rf}}^2)\Omega_R^2\Omega_{\text{rf}}^3}{288\pi\Gamma\gamma(\gamma^2 + \Delta_{\text{rf}}^2)^{3/2}(\gamma^2 + 4\Delta_{\text{rf}}^2)} + O[\Omega_{\text{rf}}]^5. \quad (14)$$

These expressions describe resonances in  $\Delta_{\text{rf}}$  centered at  $\Delta_{\text{rf}} = 0$ . To lowest order in  $\Omega_{\text{rf}}$ , they are proportional to the real part, imaginary part, and absolute value, respectively, of a complex Lorentzian. Additional features appear at higher orders, as discussed in the next section.

When  $\Omega_{\text{rf}}$  becomes of the same order as or exceeds  $\Omega_L$ , the rotating-wave approximation for the rf field is no longer valid. In this case we use the Hamiltonian  $H$  of Eq. (1) and proceed in the laboratory frame. The Liouville equation is now time dependent; periodic solutions can be found by expanding the density matrix in Fourier series and retaining a finite number of harmonics. This provides a linear system of time-independent equations that can be solved numerically for the Fourier coefficients. The observed optical rotation signals can then be found as before.

### 3. Discussion

The predictions of the density-matrix calculation described in Sec. 2.2 are compared to the experimental data in Fig. 2. For each value of the rf field strength (characterized by the rf Rabi frequency  $\Omega_{\text{rf}}$ ), the in-phase and quadrature components and the magnitude of the optical-rotation signal as a function of the rf frequency  $\omega_{\text{rf}}$  are shown. The version of the theoretical treatment valid for arbitrary rf-field strength discussed in Sec. 2.2 is used to generate the theoretical predictions, although for the lowest rf power, the signal is well described by the lowest-order terms of the expansions (12)–(14). Three regimes in the dependence on  $\Omega_{\text{rf}}$  can be identified. At the lowest field strengths,  $\Omega_{\text{rf}} < \gamma$ , the in-phase and quadrature resonances in rf frequency take the form of dispersive and absorptive Lorentzians of characteristic width  $\gamma$  (Fig. 2a). At intermediate field strengths,  $\gamma < \Omega_{\text{rf}} < |\Omega_L|$  (we assume  $\gamma \ll |\Omega_L|$ ), the Lorentzians broaden and additional narrow features are seen at the center of the resonances (Fig. 2b), the result of polarization-averaging effects discussed below.

For higher fields,  $\Omega_{\text{rf}} > |\Omega_L|$ , effects due to ac Zeeman shifts and far-off-resonant fields are predicted to become important. We did not perform measurements in this regime, but the beginning of these effects can be seen in the data (Fig. 2c). The negative-frequency component of the rf field results in a resonance at  $\omega_{\text{rf}} = -\Omega_L$  symmetric to the one at  $\omega_{\text{rf}} = \Omega_L$ . In Fig. 2(b) and (c), the off-resonant tail of this negative-frequency resonance produces an overall slope in the in-phase component of the positive-frequency signal. Calculations for values of  $\omega_{\text{rf}}$  of the same order as  $\Omega_L$  predict higher-order resonances at odd fractions (1/3, 1/5, etc.) of  $\Omega_L$ . When the experimental data presented in Fig. 2(c) are plotted on expanded scales, as in Fig. 3, a higher-order resonance can be observed at one third the frequency of the main resonance, in agreement with theoretical predictions.

#### 3.1. Low-field regime

We first consider the low-rf-field regime,  $\Omega_{\text{rf}} < \gamma$ . This case was discussed in Ref. [15]. An example of experimental data taken in this regime compared to theoretical predictions is shown



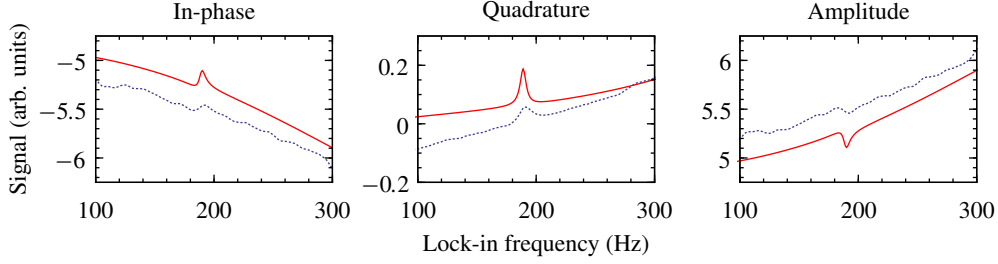


Fig. 3. Row (c) of Fig. 2 plotted on expanded scales. (The vertical scale is different for each plot.) A resonance due to high-field effects can be seen near  $\omega_{\text{rf}}/(2\pi) = \frac{1}{3}\Omega_L/(2\pi) \approx 185$  Hz.

in Fig. 2(a). As described by Eqs. (12)–(14), the resonance observed in the in-phase component, quadrature component, and magnitude of the optical-rotation signal takes the form of the real (dispersive) part, imaginary (absorptive) part, and the magnitude of a complex Lorentzian, respectively. The absolute value of a complex Lorentzian has the line shape of the square root of the absorptive part. Near resonance the quadrature component is the primary contributor to the magnitude, while farther from resonance, the in-phase component provides the main contribution. The characteristic width of the observed resonances is determined by the ground-state relaxation rate.

Optical pumping by the light field removes atoms from the  $m_g = 0$  sublevel, leaving an incoherent mixture of atoms in the  $m_g = \pm 1$  sublevels. The atomic polarization can be illustrated using the angular-momentum-probability surface (AMPS) [26, 27, 28], whose radius in a given direction is determined by the probability of measuring the maximum possible angular-momentum projection in that direction. This provides the quantum-mechanical analog of the classical angular-momentum probability distribution. The optically pumped distribution corresponds to atomic alignment along the  $z$ -axis with a “peanut”-shaped probability distribution (Fig. 4a). (All of the AMPS shown here are obtained directly from the density-matrix calculation. A quantity of the lowest-rank, isotropic polarization moment is subtracted from each figure so that the anisotropic polarization can be more clearly seen [28].) Because the  $m_g = 0$  sublevel has been depleted, the atomic medium transmits  $z$ -polarized light, while tending to absorb orthogonally polarized light—i.e., the atoms function as a polarizing filter with transmission axis along the atomic alignment axis [29]. This linear dichroism can induce rotation of the light polarization if the transmission axis is tilted away from the light polarization axis.

The observed signals in the low- and intermediate-field regimes can be most readily understood in terms of Larmor precession of the atomic alignment in the combined static and rf magnetic field. In the rotating frame, under the rotating-wave approximation for the rf field, the effect of the magnetic fields  $\mathbf{B}_0$  and  $\mathbf{B}_{\text{rf}}$  can be described in terms of fictitious static fields  $\mathbf{B}'_0$  and  $\mathbf{B}'_{\text{rf}}$ . These fields can be determined by examining the rotating-frame Hamiltonian (3). The bias field in the rotating frame,  $\mathbf{B}'_0$ , points along  $\mathbf{B}_0$ , while its field strength is such that it produces a Larmor frequency given by the detuning of the rf field from resonance:  $\Omega'_L = -\Delta_{\text{rf}} = -\omega_{\text{rf}} + \Omega_L$ . The rf field  $\mathbf{B}_{\text{rf}}$  becomes a static field  $\mathbf{B}'_{\text{rf}}$  in the  $xy$  plane with associated Larmor frequency  $\Omega'_{\text{rf}} = \Omega_{\text{rf}}/2$ . The direction of this field in the  $xy$  plane depends on the arbitrary phase chosen for the rotating frame; in our convention  $\mathbf{B}'_{\text{rf}}$  points along  $\hat{\mathbf{x}}$ . Thus the resultant field  $\mathbf{B}'_{\text{tot}} = \mathbf{B}'_0 + \mathbf{B}'_{\text{rf}}$  lies in the  $xz$  plane.

The atomic polarization evolves in the rotating frame under the action of  $\mathbf{B}'_{\text{tot}}$ . For low field strengths, this evolution is Larmor precession, so that the polarization continues to correspond to alignment. Because all of the external fields are static in the rotating frame, the effect of

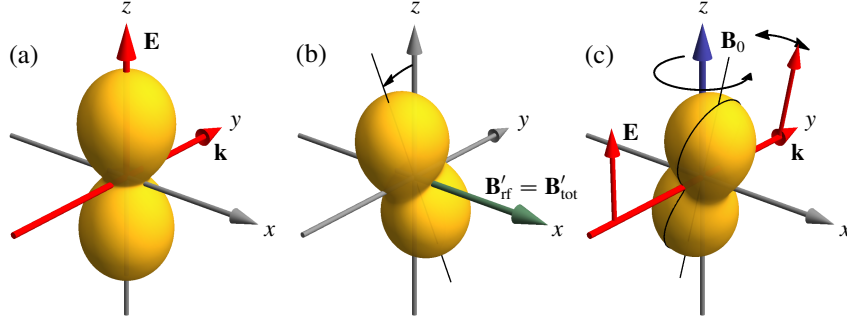


Fig. 4. Angular-momentum-probability surfaces illustrating the behavior of the system with a resonant ( $\Delta_{\text{rf}} = 0$ ), weak rf field. (a) The light, with electric field  $\mathbf{E}$ , produces atomic alignment along the  $z$ -axis. (b) In the rotating frame, the atoms precess around the  $x$ -axis. Due to relaxation, a steady state is reached. (c) In the laboratory frame, the atoms precess around the  $z$ -axis, with the linear dichroism of the ensemble inducing oscillating optical rotation in the  $z$ -polarized,  $\hat{\mathbf{y}}$ -propagating light field. (Media 1 animates the precession and optical rotation as a function of time.) The transmission axis of the polarized ensemble, in this case parallel to the atomic alignment axis, is indicated with a line drawn on the surface.

relaxation leads to a steady state for the atomic polarization. First consider the case in which the rf field is exactly on resonance ( $\Delta_{\text{rf}} = 0$ ). Then  $\mathbf{B}'_{\text{tot}}$  is equal to  $\mathbf{B}'_{\text{rf}}$  and points in the  $\hat{\mathbf{x}}$  direction (Fig. 4b), and the atomic alignment precesses in the  $yz$  plane. Under the assumption  $\Omega_{\text{rf}} \ll \gamma_l$ , the precession frequency is much less than the relaxation rate, so that each atom precesses through a small angle before relaxing. The rotating-frame steady-state ensemble polarization thus consists of alignment at a small angle to the  $z$ -axis in the  $yz$  plane (Fig. 4b).

In the laboratory frame, the alignment precesses about the  $z$ -axis (Fig. 4c). At the instant that the alignment is in the  $yz$  plane, it does not induce any polarization rotation in the  $\hat{\mathbf{y}}$ -propagating light field. On the other hand, whenever the alignment axis is tilted away from the initial light polarization axis (the  $z$ -axis) in the plane transverse to the light propagation direction (the  $xz$  plane), the atoms can induce optical rotation. Because of the precession of the alignment, the optical-rotation signal oscillates. The amplitude of the signal is determined by the amount of the alignment and the angle between the alignment axis and the  $z$ -axis (zenith angle). The phase of the oscillating signal is determined by the angle of the alignment axis about the  $z$ -axis in the rotating frame (azimuthal angle). The direction of the alignment axis in the rotating frame corresponds to its direction in the laboratory frame when the rf field is maximum. Only the component in the  $xz$  plane will induce optical rotation in  $y$ -propagating light, so an alignment axis in the  $xz$  plane in the rotating frame produces a signal in phase with the rf field oscillation, while the component in the  $yz$  plane produces a quadrature component in the signal. In the case of Fig. 4 the optical-rotation signal is entirely in the quadrature component.

As the rf field is tuned away from resonance, the total field in the rotating frame begins to point away from the  $x$ -axis and toward the  $z$ -axis. Precession about this field then takes the alignment in the rotating frame out of the  $yz$  plane (Fig. 5a). This tends to reduce the angle that the steady-state alignment makes with the  $z$ -axis, reducing the amplitude of the laboratory-frame optical rotation signal. On the other hand, because the alignment now has a component in the  $xy$  plane in the rotating frame, the oscillating rotation signal gains an in-phase component. When the rf field is tuned far enough away from resonance so that  $|\Delta_{\text{rf}}| > \gamma_l$ , the precession frequency in the rotating frame becomes large enough that the atoms undergo an entire precession cycle before relaxing. The ensemble polarization is then averaged about the direction of the

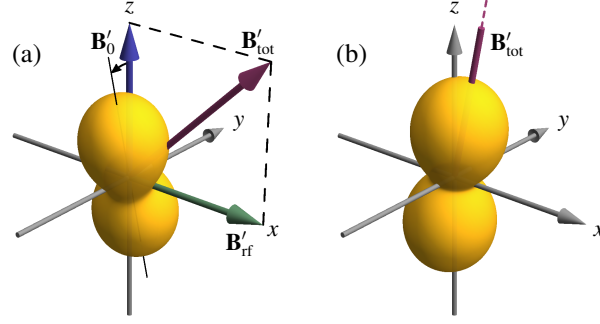


Fig. 5. As Fig. 4, but with an off-resonant rf field. (a) In the rotating frame, the atoms precess around the total effective field, which lies in the  $xz$  plane. As a result, the polarization is no longer entirely in the  $yz$  plane. (b) Far off resonance, the effective magnetic field is large enough that the polarization is completely averaged about the magnetic-field direction. (The arrow representing  $\mathbf{B}'_{\text{tot}}$  is truncated, as it is too long to fit entirely on the plot.) Media 2 shows the polarization, along with the in-phase component of the optical-rotation signal, as the rf-field detuning is swept through resonant and off-resonant conditions

total magnetic field (Fig. 5b). Because  $\mathbf{B}'_{\text{tot}}$  lies in the  $xz$  plane, the signal is now predominately in phase with the rf field, and the quadrature component is strongly suppressed. As the detuning becomes large, the average polarization points more and more along the  $z$ -axis, and the signal amplitude drops to zero.

The preceding description is seen to correspond to the signals shown in Fig. 2(a)—the dispersive (in-phase) and absorptive (quadrature) components and the magnitude of a Lorentzian with characteristic width  $\gamma_l$ —as well as to the lowest order terms of Eqs. (12)–(14).

### 3.2. Intermediate-field regime

When the rf field is large enough that  $\gamma_l < \Omega_{\text{rf}} < |\Omega_L|$ , the rotating-frame precession frequency is high even at zero detuning. This causes averaging of the atomic polarization about the magnetic-field axis. For  $\Delta_{\text{rf}} = 0$  this is the  $x$ -axis: polarization transverse to the  $x$ -axis is averaged out. However, the polarization along the  $x$ -axis is preserved, so that the  $x$ -axis becomes the preferred axis for the polarization (Fig. 6a). The “doughnut”-shaped probability distribution seen in Fig. 6(a) is obtained from the initially pumped “peanut”-shaped distribution (Fig. 4a) when copies of the peanut distribution rotated by arbitrary angles about the  $x$ -axis are averaged together. Another way to explain the doughnut shape is to transform to the basis in which the quantization axis is along  $\hat{\mathbf{x}}$ . In this basis, the excitation light is  $\sigma$  polarized, so that it pumps atoms out of the bright state consisting of a superposition of the  $m_g = \pm 1$  sublevels, and leaves them in the dark state made up of the opposite superposition, as well as in the  $m_g = 0$  sublevel. However, due to the precession induced by the  $\hat{\mathbf{x}}$  directed magnetic field, atoms oscillate between the bright and dark superpositions, so that the pump light removes atoms from the  $m_g = \pm 1$  sublevels incoherently. The atoms are then left in the  $m_g = 0$  sublevel, i.e., the atoms have no angular-momentum projection on the  $x$ -axis and are symmetric about the  $x$ -axis, as seen in Fig. 6(a).

Polarization along the  $x$ -axis remains in the  $xy$  plane as it precesses around the  $z$ -axis in the laboratory frame and so does not induce any optical rotation. However, when the rf field is tuned slightly away from resonance,  $\mathbf{B}'_{\text{tot}}$  points away from the  $x$ -axis, and so also does the averaged atomic polarization (Fig. 6b). The polarization then causes optical rotation. As the polarization in the rotating frame is in the  $xz$  plane, the signal in the laboratory frame is in phase with the rf field. (The plots in Fig. 6 are shown for the instant at which the rotating frame coincides with

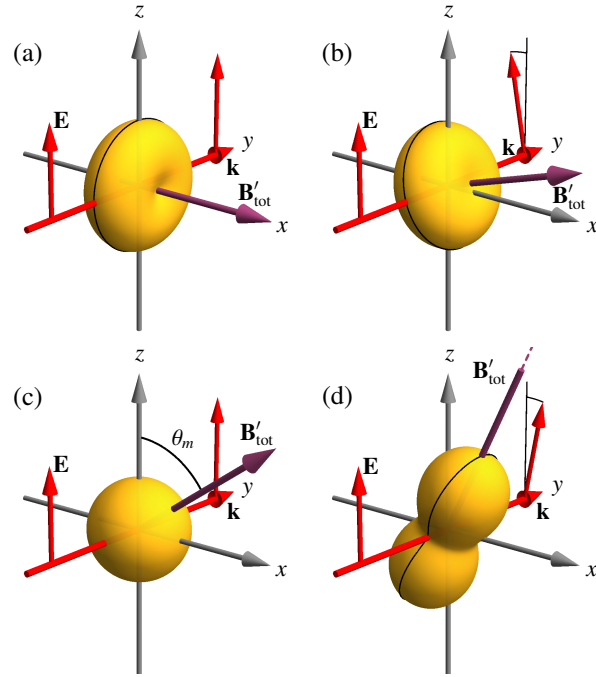


Fig. 6. Rotating-frame AMPS for intermediate rf field strength, in the ideal case in which  $\gamma \ll \Omega_{\text{rf}} \ll |\Omega_L|$ . Optical rotation is indicated for the instant in which the rotating frame coincides with the laboratory frame—this means that the generation of the in-phase component of the signal is shown. (a) When the rf field is on resonance, the atomic polarization (created along the  $z$ -axis) is averaged about the  $x$ -axis. The resulting polarization is a “doughnut” aligned along the  $x$ -axis. The transmission axis, perpendicular to the alignment axis, is marked with a line on the surface. (b) For small detunings, the alignment axis follows the effective magnetic field direction. (c) When the effective magnetic field is at the magic angle  $\theta_m = \arccos(1/\sqrt{3})$  to the light polarization direction, the atomic polarization is completely averaged out due to precession. (d) For larger detunings, the polarization regains its original “peanut” shape, and the transmission axis is along the alignment axis. Media 3 shows the atomic polarization and in-phase optical rotation as the rf-field detuning is swept through resonance.

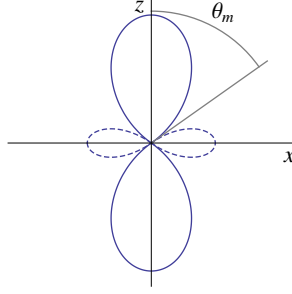


Fig. 7. Cross section of the AMPS for pure alignment along the  $z$ -axis, described by  $Y_{2,0}(\theta, \phi) \propto 3 \cos^2 \theta - 1$ . Positive function values are shown as solid lines, negative function values as dashed lines. The magic angle  $\theta_m = \arccos(1/\sqrt{3})$  is indicated.

the laboratory frame, so that the in-phase component of the optical rotation is shown.)

To understand the generation of optical rotation in this case, it is important to note the effect of the different character of the ensemble polarization. In the low-field case, the angular-momentum probability distribution has maxima along the ensemble polarization axis (a peanut), while in the current case, the distribution has minima (a doughnut). (This result depends on the particular type of transition considered—for a  $F_g \rightarrow F_e = F_g$  transition the situation is reversed.) We can think of the doughnut shape as an unpolarized distribution (sphere) with a peanut shape removed. From this viewpoint, it is reasonable that this “negative polarization” produces rotation of the opposite sign. More concretely, we can note that, as described above, in a doughnut distribution atoms are concentrated in the  $m_g = 0$  sublevel with the quantization axis along the alignment axis. The state then preferentially absorbs light that is polarized along the alignment axis. In the analogy with a polarizing filter, the transmission axis of the doughnut-shaped probability distribution is transverse to, rather than along, the alignment axis. This explains the sign of the rotation shown in Fig. 6(b) when  $\mathbf{B}'_{\text{tot}}$  points away from the  $x$ -axis. (The transmission axis of each polarization state is marked with a line on the surfaces plotted in Fig. 6.)

As the rf field is tuned farther from resonance,  $\mathbf{B}'_{\text{tot}}$  points farther away from the  $x$ -axis, bringing the averaged alignment axis with it. This larger angle produces a larger optical rotation signal. However, another trend eventually takes over: because of the shape of the initially pumped polarization distribution, the amount of polarization that lies along the magnetic-field direction decreases. As a result, the amount of averaged polarization is reduced, tending to reduce the signal. In order to analyze this, we can plot just the aligned part of the initially pumped density matrix, neglecting the isotropic part that is included in Fig. 4(a). The surface corresponding to just the rank  $\kappa = 2$ ,  $q = 0$  polarization moment is described by the spherical harmonic  $Y_{2,0}(\theta, \phi) \propto 3 \cos^2 \theta - 1$ , plotted in cross section in Fig. 7. Negative values of the function are indicated by dashed lines. There are maximum positive values along  $z$  ( $\theta = 0$ ), and maximum negative values in the  $xy$  plane ( $\theta = \pi/2$ ). As  $\theta$  moves away from either of these values, the magnitude of the polarization is reduced. At a particular angle  $\theta_m = \arccos(1/\sqrt{3})$ , analogous to the magic angle observed in nuclear magnetic resonance experiments, the polarization moment goes to zero. This means that if  $\mathbf{B}'_{\text{tot}}$  is at this angle to the  $z$ -axis, the averaged polarization completely cancels, sending the optical rotation signal to zero (Fig. 6c). This condition corresponds to the additional zero crossings seen in the in-phase component of Fig. 2(b,c) above and below the center of the resonance. The direction of the effective magnetic field in the rotating frame depends on the rf field strength and the detuning from resonance—as the field strength is increased, the detuning required to achieve the magic angle also increases.

When the detuning is even larger, there is once again residual polarization after averaging about the magnetic-field direction. However, now the magnetic-field direction is close enough to the initial alignment axis that the polarization resulting from averaging resembles the peanut shape of the initially pumped polarization (Fig. 6d). Thus, the optical-rotation signal in this case is opposite in sign to that for small detuning and has the same sign as that for the low-power case.

As the detuning continues to increase,  $\mathbf{B}'_{\text{tot}}$  and the averaged atomic alignment point more toward the  $z$ -axis, reducing the optical-rotation signal.

The preceding discussion describes the in-phase signal shown in Fig. 2(b) and (c): a power-broadened Lorentzian with a narrower feature of the opposite sign in the center. If the discussion is strictly interpreted, there should be no quadrature signal in this regime, as the polarization in the rotating frame is always in the  $xz$  plane. Figure 2 does display (strongly suppressed) quadrature signals, which are a remnant of the low-field regime.

### 3.3. High-field regime

As  $\Omega_{\text{rf}}$  becomes of the same order as  $\Omega_L$  or exceeds it, various higher-order effects appear in the data and the full theory that cannot be described under the rotating-wave approximation for the rf field. In particular, a resonance near  $\Omega_L/3$  is seen, as shown in Fig. 3. This can be explained as due to ac Zeeman shifts, which produce evenly spaced sidebands that result in resonances at odd subharmonics of the lowest-order resonance. The additional features can also be interpreted as arising from higher-order resonances between the Larmor precession and the rf frequency, similar to those seen in nonlinear magneto-optical rotation with frequency-modulated light [30]. As the rf field strength increases, many additional resonances are predicted by the theory.

## 4. Conclusion

We have conducted a detailed experimental and theoretical investigation of magneto-optical rotation in the presence of a strong radio-frequency field. A model has been developed that allows both the reproduction of the nontrivial line shapes that appear as the rf field strength is increased, and also the qualitative understanding of the atomic polarization dynamics responsible for the signals. The results of this study will be useful for the analysis of the behavior of atomic magnetometers exposed to strong radio-frequency fields. The results may also have applications in the design of efficient methods for the preparation of specific polarization states of atoms, for example, atomic states with large alignment but no orientation, as are used in the work of Ref. [19].

## Acknowledgments

We are grateful to M. P. Ledbetter for his help with the experimental setup. This research was supported by Grant No. 2006220 from the United States-Israel Binational Science Foundation (BSF) and by the ONR MURI and NGA NURI programs. S.G. and E.J.B. were undergraduate exchange students at the University of California at Berkeley while working on this project.